nature communications

Article

https://doi.org/10.1038/s41467-026-69260-z

Engineering *d*-orbital of copper single-atom sites toward industrial-level electrocatalytic methanation

Received: 23 August 2025

Accepted: 28 January 2026

Published online: 13 February 2026

Check for updates

Zhengzheng Liu[1,2,6], Junzhuo Cai[3,6], Shuming Dong[1], Chaoxiu Qin[1], Zhuoran Lv[4], Yu Yang[5], Jiacheng Jayden Wang[4], Jiaxu Gong[4], Huibin Zhang[1], Huazhen Cao[1], Anxiang Guan[2], Zhangliu Tian[4], Qing Han[2] ✉, Fengwang Li[5], Fuqiang Huang[4] ✉, Ximeng Lv[2,4] ✉ & Guoqu Zheng[1] ✉

Copper (Cu)-based single-atom catalysts (SACs) enable electrocatalytic CO_2 reduction into methane (CH_4) fuel for thermal power plant decarbonization, yet conventional Cu SACs face industrial deployment barriers like instability and sluggish kinetics caused by $d-p$ orbital coupling. Herein, we develop a Cu–Ti_1O_3 catalyst with localized Cu single-atom sites by oxygen vacancy (O_v)-involved orbital engineering, achieving industrial-level CH_4 production. Theoretical and in-situ studies reveal the intensification of the $d-d$ coupling at Cu sites triggered by [Cu–O_v – Ti] motifs, which enhances d-π* polar interactions upon $*CO_2$ and accelerates C – O bond cleavage in $*OCH_3$ intermediate. As a result, Cu–Ti_1O_3 achieves a competitive performance, i.e., the highest Faradaic efficiency of 76% and a peak partial current density of 670 mA cm^{-2} toward CH_4 (corresponding turnover frequency = 24,930 h^{-1}), ~3.5-fold promotion over conventional Cu SACs. Furthermore, it demonstrates high durability (>1,230 hours) at an industrial-level current density, exceeding the longevity of conventional Cu SACs by over 20 times. Our findings highlight the prospect of *d*-orbital engineering in enabling industrial-level electrocatalytic methanation, offering promising implications for decarbonizing traditional power plants.

Carbon emissions from traditional thermal power plants significantly hinder carbon neutrality efforts, e.g., overseas coal-fired power plants currently emit 0.53 gigatons of CO_2 per year[1]. To address this, abundant decarbonization technologies are being proposed, among which the electrocatalytic CO_2 reduction reaction (CO_2RR) emerges as a critical pathway for CO_2 valorization and sustainable fuel production[2,3]. Specifically, electro-catalytic methanation (i.e., CO_2-to-CH_4 conversion) using flue gas provides a promising decarbonization strategy by coupling CO_2 fixation with high-energy CH_4 (55.5 MJ kg^{-1}) production for thermal power plants[4,5]. Regarding catalyst candidates, copper (Cu)-based catalysts facilitate pathways for deeply reduced products, including CH_4 (>2e^- transfer)[6,7], but face challenges of sluggish kinetics ($|J_{total}|$ <500 mA cm^{-2}) and poor selectivity (<50%).

From a mechanistic perspective[8,9], spatially coupled Cu–Cu sites promote C–C coupling over the CH_4 pathway (e.g., 0.53 eV higher

[1]College of Materials Science and Engineering, Zhejiang University of Technology, Hangzhou, China. [2]Laboratory of Advanced Materials, Department of Chemistry and Shanghai Key Laboratory of Molecular Catalysis and Innovative Materials, Fudan University, Shanghai, China. [3]College of Environmental Sciences, Sichuan Agricultural University, Chengdu, China. [4]State Key Lab of Metal Matrix Composites, School of Materials Science and Engineering, Shanghai Jiao Tong University, Shanghai, China. [5]School of Chemical and Biomolecular Engineering and ARC Centre of Excellence for Green Electrochemical Transformation of Carbon Dioxide, The University of Sydney, Sydney, NSW, Australia. [6]These authors contributed equally: Zhengzheng Liu, Junzhuo Cai. ✉e-mail: qhan@fudan.edu.cn; huangfq@sjtu.edu.cn; ximeng_lv@fudan.edu.cn; zhenggq@zjut.edu.cn

https://doi.org/10.1038/s41467-026-69260-z

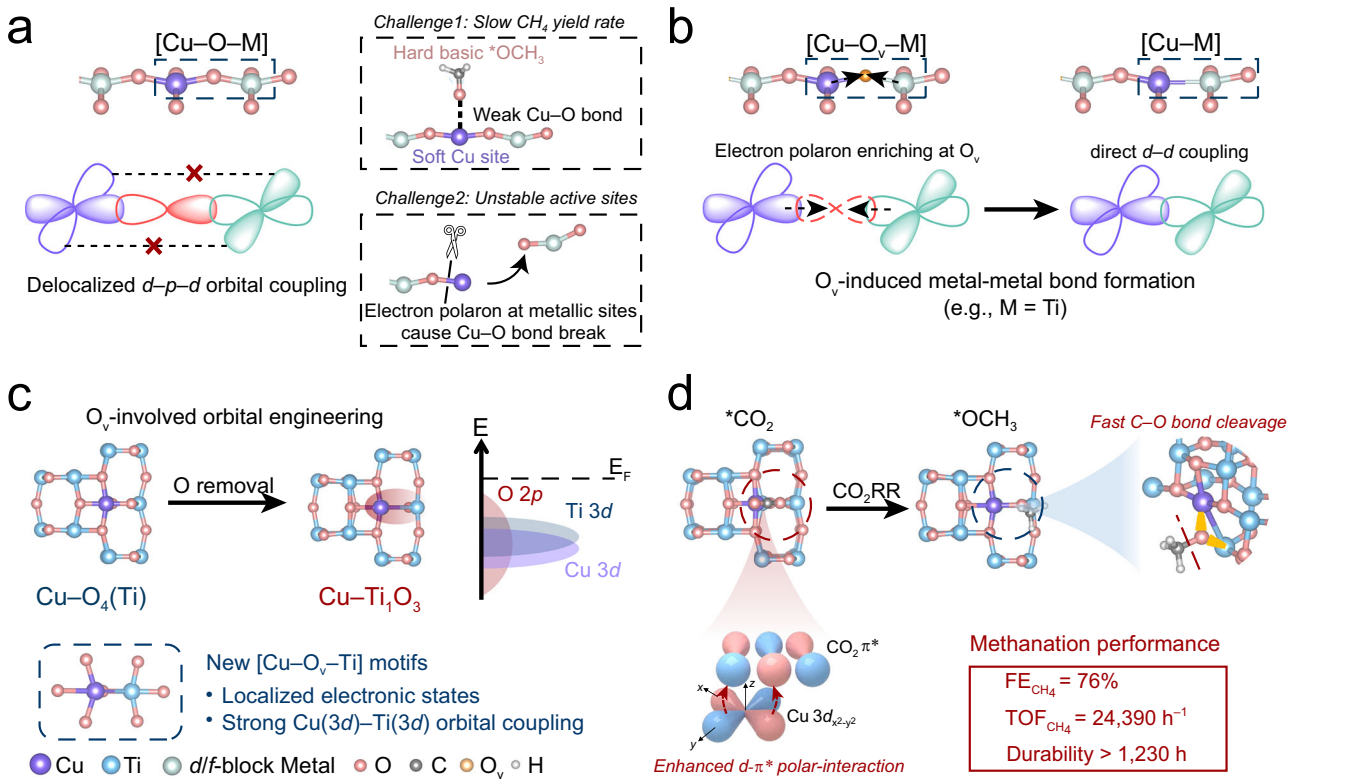

Fig. 1 | Schematic illustration of orbital engineering on Cu single-atom catalysts. a Conventional Cu_1/MO_x SACs display a delocalized *d–p–d* orbital coupling involving lattice oxygen, causing two major challenges: sluggish kinetics and instability. **b** Electron-polaron accumulation at O_v sites induces strong *d–d* orbital coupling in a valent-variable system like Cu_1/TiO_x. **c** Synthesis of $Cu–Ti_1O_3$ via lattice O removal in Cu-embedded TiO_2, obtaining a localized [Cu–O_v – Ti] motif with strong *d–d* orbital coupling. **d** $Cu–Ti_1O_3$ achieves enhanced d-π* polar interactions on $*CO_2$ and accelerated C–O bond cleavage of $*OCH_3$, thereby leading to highly efficient and stable CH_4 production.

barrier for CH_4 on bulk Cu[10]). Therefore, enhancing CH_4 selectivity requires spatially isolated Cu single-atom catalysts (SACs). Current synthesis strategies for Cu SACs rely on embedding Cu into non-metallic matrices like carbon, C_3N_4, and so on (Supplementary Fig. 1a)[6]. For instance, N-coordinated Cu SACs have been confirmed to own a favored C_1 selectivity (e.g., CO[11], HCOOH[12], and CH_4[13,14]). Nevertheless, the modern hard-soft acid-base (HSAB) theory[15,16] illustrates that the inherently delocalized *p*-orbitals[17] may cause a *d*-electronic delocalization via *d–p* orbital coupling, thus weakening hard-basic intermediate adsorption like $*OCH_3$ and facilitating hydrogen evolution side reaction[18] at Cu sites (Details in Supplementary Note 1)[15]. Moreover, Cu–X (X=C, N, O) coordinates are thermodynamically unstable[19], causing severe reconstruction such as agglomeration of Cu atoms. This may facilitate C–C coupling[20] and cause performance degradation under industrial-level current density (> 500 mA cm^{-2})[21].

To these issues, constructing localized Cu single-atom sites (i.e., harder acid[15]) by introducing matrices with localized *d/f* valence orbitals may be essential[22], and proposed solutions include constructing Cu_1M single-atomic alloys (M = *f/d*-block elements) as well as Cu_1/MO_x SACs (Supplementary Fig. 1b, c). Although Cu_1M systems feature localized *d*-orbitals, free-atom-like Cu sites (i.e., resembling *d–p* coupled molecular metal complexes) will cause an unstable condition[23,24], thus favoring a tight *CO binding and predominant CO selectivity[25]. For Cu_1/MO_x SACs, the intrinsic charge polarization of M–O bonds[26] and spin-orbit interaction triggered insurmountable energy barriers for direct *d–d/f* coupling[27,28], finally causing dominative [Cu–O–M] motifs that facilitate indirect *d–p–d/f* coupling during catalyst synthesis[29,30]. In this indirect *d–p–d/f* coupling structure, the continuous electron-polaron accumulation at *d*-orbitals during CO_2RR may destroy the Cu –O coordinates[31], significantly threatening the robustness (Fig. 1a). For instance, Zhou et al. synthesized a Cu-Ce-O_x catalyst (i.e., *d–p–f* coupling) with isolated Cu sites[32], achieving an efficient CO_2-to-CH_4 conversion (FE of CH_4 (FE_{CH_4}) ≈ 65%), but durability remains poor (<10 h). Unlike typical electron-polaron trapping at metallic sites, electron in anatase titanium oxide (TiO_2) prefers a free-carrier state, and can only be trapped at oxygen vacancy (O_v)[31,33], providing a vital opportunity for O_v-induced metal-metal bond formation (strong *d–d* coupling, Fig. 1b), thereby constructing localized Cu single-atom sites (*l*-Cu sites) and stabilizing the active sites[34,35]. Inspired by these, employing O_v-rich TiO_2 as matrices may be a promising strategy to realize strong *d–d* coupling and facilitate selective and stable methanation.

Herein, we have developed an oxygen-vacancy-involved orbital engineering method to construct [Cu–O_v–Ti] motifs through O removal in Cu-embedded TiO_2 SAC (Fig. 1c). As-synthesized Cu-based SAC (marked as $Cu–Ti_1O_3$) achieves an efficient CO_2-to-CH_4 conversion in flow cells, including an excellent $FECH_4$ of 76% at −0.88 V (potentials converting into the reversible hydrogen electrode (RHE), see "Methods"), and a record-high turnover frequency of CH_4 to date (24,390 h^{-1} at −1.0 V). Furthermore, $Cu–Ti_1O_3$ also exhibits exceptional stability of >1230 h at an industrial-level current density (600 mA cm^{-2}) in a zero-gap electrolyzer, over 12 times longer than a conventional Cu_1/TiO_2 catalyst with major [Cu–O–Ti] motifs (marked as $Cu–O_4(Ti)$). Synergistic experimental/theoretical analyses reveal that O_v-intensified *d–d* orbital coupling between Cu and Ti atoms enhances electronic localization of $Cu^{\delta+}$ sites (i.e., harder acidity than pristine $Cu^{\delta+}$ sites in $Cu-O_4(Ti)$), strengthening *d*-π* polar interactions with adsorbed $*CO_2$ (Fig. 1d) and stabilizing the Cu–O binding with hard-basic $*OCH_3$. Simultaneously, in-situ time-field electrochemical electron magnetic resonance (E-EMR) reveals a new mechanism involving pseudo-lattice oxygen formation through $*OCH_3$ insertion into O_v. This reversible

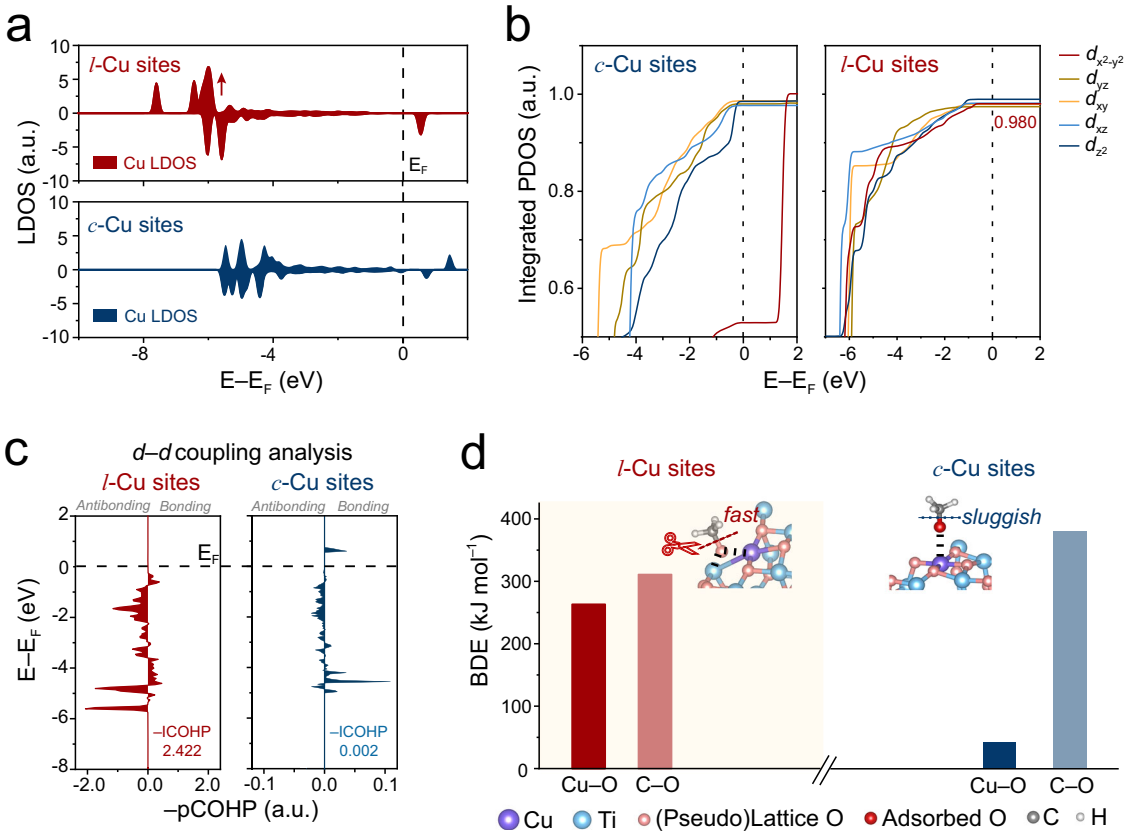

Fig. 2 | Assessments on the electronic states of two distinct Cu single-atom site configurations. a LDOS of Cu atom at *l*-Cu and *c*-Cu sites. **b** IPDOS of Cu–O–Ti and *l*-Cu sites around the Fermi level. **c** COHP analysis for *d*–*d* orbital coupling at *c*-Cu and *l*-Cu sites. **d** BDE evaluations illustrate that strong *d*–*d* coupling promotes C–O bond cleavage of $*OCH_3$ on *l*-Cu sites compared with *c*-Cu sites. Source data for Fig. 2 are provided as a Source Data file.

pseudo-lattice oxygen formation route supplements a localized ultra-stable adsorption for $*OCH_3$ surpassing the typical physico/chemical adsorption at conventional Cu single-atom sites (*c*-Cu sites) with majorly Cu–O coordination (i.e., bond dissociation enthalpy (BDE) of Cu–O = 263.1 vs. 41.9 kJ mol^{-1}). Therefore, an accelerated C–O bond cleavage (-16.8% lower BDE) and rapid methanation generation on Cu–Ti_1O_3 are achieved compared with Cu-O_4(Ti) (Supplementary Fig. 2). Overall, this work establishes an orbital engineering method for constructing localized Cu single-atom sites and provides a universal strategy to design durable SACs toward industrial-level CO_2-to-fuel conversion.

Results

Synthesis and characterization

Density functional theory (DFT) calculations were first employed to evaluate the influence of *d*–*d* orbital coupling at Cu single-atom sites. The local density of states (LDOS) for Cu atom at [Cu–O_v–Ti] motifs exhibits intensified peaks relative to the conventional [Cu–O–Ti] structures, confirming localized electronic states of *l*-Cu sites (Fig. 2a, Supplementary Fig. 3). Integrated projected density of states (IPDOS) analysis identifies the $d_{x^2-y^2}$ orbital as the frontier orbital of the Cu sites (Supplementary Fig. 4). The higher electron density within the $d_{x^2-y^2}$ orbital (e.g., IPDOS = 0.980 for up-spin states, Fig. 2b and Supplementary Table 1) of *l*-Cu site likely facilitates strong *d*-π* polar-interactions on adsorbed $*CO_2$, corroborating accelerated CO_2 activation[36,37], and leading to an enhanced CO_2-to-CH_4 conversion trend as reported by Huang's group[37]. Furthermore, crystal orbital Hamilton population (COHP) analyses reveal a significantly larger negative integrated COHP (−ICOHP) value for the Cu–Ti bond on *l*-Cu sites (2.422 a.u.) versus *c*-Cu sites (0.002 a.u., Fig. 2c), indicating robust *d*–*d* coupling induced by oxygen vacancies. BDE assessments of $*OCH_3$ confirm tighter Cu–O bonding post orbital engineering (BDE_{Cu-O} = 263.1 kJ mol^{-1} on *l*-Cu sites, Fig. 2d) compared with unstable adsorption on pristine *c*-Cu sites (BDE_{Cu-O} = 41.9 kJ mol^{-1}, Supplementary Table 2). Meanwhile, a 16.8% reduction in BDE_{C-O} at *l*-Cu sites suggests potential acceleration of C–O bond cleavage during CO_2RR (inset slab model in Fig. 2d). Hence, *d*–*d* orbital coupling at *l*-Cu sites confers a kinetically enhanced methanation pathway.

Guided by computational insights, we designed Cu–Ti_1O_3 SAC with partial Cu–Ti bonding toward CO_2RR. In detail, Cu single-atom precursor was first fabricated through a hydrothermal method (Details in "Methods"), where Cu substitutes Ti in [TiO_6] octahedra and forms Cu–O–Ti motifs[38]. Given that lattice oxygen removal facilitates adjacent metallic bonding[39,40], Cu single-atom precursor was then calcined in 10% H_2/Ar for 3 h (surface Cu: 2.67 wt%, Supplementary Table 3) to synthesize Cu–Ti_1O_3. As a control group, Cu–O_4(Ti) catalyst was prepared by an air-calcination of Cu single-atom precursors. X-ray diffraction (XRD) patterns confirmed the major anatase phase (PDF#71-1167, Supplementary Fig. 5a) in Cu–Ti_1O_3, while Cu-related peaks were absent, indicating the lattice incorporation of Cu atoms. Compared to pristine TiO_2, the (101) diffraction peak of Cu–Ti_1O_3 shifted to a smaller angle, which might result from the lattice expansion[38]. Meanwhile, Cu–Ti_1O_3 exhibited a higher 2θ angle for the (101) plane than Cu–O_4(Ti), suggesting the lattice shrinkage caused by O_v accumulation (Supplementary Fig. 5b)[41].

The morphologies and atomic structures of Cu–Ti_1O_3 and Cu–O_4(Ti) were then examined by transmission electron microscopy (TEM) and aberration-corrected high-angle annular dark-field scanning transmission electron microscopy (HAADF-STEM). The TEM images illustrated a retained TiO_2 particle size of ~20 nm after Cu embedding

https://doi.org/10.1038/s41467-026-69260-z

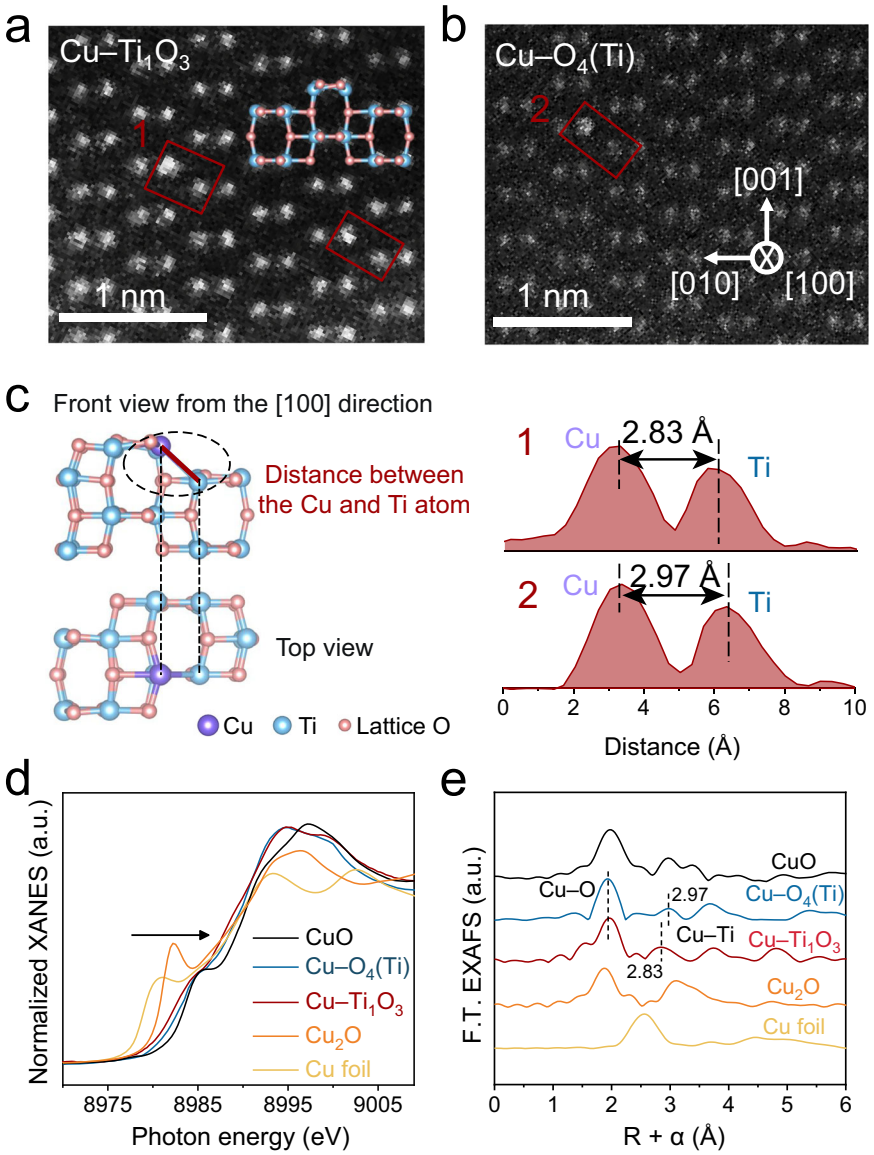

Fig. 3 | Structural characterization of Cu single-atom catalysts. Aberration-corrected HAADF-STEM images of **a** Cu–Ti_1O_3 and **b** Cu–O_4(Ti) along the [100] direction. **c** Left panel: Front and top views of Cu–Ti_1O_3, where the purple, blue, and red spheres represent the Cu, Ti, and O atoms, respectively. Right panel: the measured distance between the adjacent Cu and Ti atoms on Cu–Ti_1O_3 and Cu–O_4(Ti). **d** Normalized XANES spectra at Cu K-edge. **e** Fourier-transformed k^2-weighted EXAFS spectra at Cu K-edge for Cu foil, Cu_2O, CuO, Cu–Ti_1O_3 and Cu–O_4(Ti) samples. Source data for Fig. 3c–e are provided as a Source Data file.

(Supplementary Fig. 6). High-resolution transmission electron microscopy (HRTEM) of the Cu–Ti_1O_3 revealed an ~0.194 nm interplanar spacing for the (200) plane (d_{200}, Supplementary Fig. 6), indicating a lattice expansion compared with TiO_2 (d_{200} = 0.189 nm). The energy-dispersive spectroscopy (EDS) mapping confirmed the uniform distribution of Cu, O, and Ti across the nanoparticles (Supplementary Fig. 7). In addition, HAADF-STEM revealed the dumbbell-shaped periodic arrays consisting of adjacent Ti atom pairs along the [100] direction in Cu–O_4(Ti) and Cu–Ti_1O_3 (Fig. 3a, b). Bright spots that refer to Cu atoms were exclusively located at the original Ti sites, indicating the on-site substitution and formation of Cu single-atom sites in Cu–Ti_1O_3 and Cu–O_4(Ti). Moreover, in the [100]-directed images (Fig. 3c), the distance between one bright (Cu) and one dark spot (Ti) in Cu–Ti_1O_3 was about 2.83 Å, shorter than that in Cu–O_4(Ti) (2.97 Å), suggesting an atom approaching and a possible direct Cu–Ti bond formation triggered by O_v.

Interfacial electronic states were then assessed by X-ray photoelectron spectroscopy (XPS). The high-resolution spectra of O 1*s* showed a higher O_v peak at 531.2 eV[42] for Cu–Ti_1O_3 than Cu–O_4(Ti) (ca. 18.5% vs. 10.8%, Supplementary Fig. 8). As for Cu 2p spectra (Supplementary Fig. 9a), Cu–O_4(Ti) catalyst showed two main deconvoluted peaks at around 951.7 eV and 932.0 eV, respectively, attributed to Cu^0/Cu^+ species[15]. These two peaks exhibited a ~0.40 eV red-shift in Cu–Ti_1O_3, demonstrating an intensified electron density at interfacial Cu sites[43]. Cu *LMM* Auger spectra unveiled that both catalysts exhibited two fitted peaks at 917.7 and 916.7 eV (Supplementary Fig. 10), ascribed to the Cu^{2+} and Cu^+ species, respectively[44]. In detail, Cu–Ti_1O_3 possessed a higher ratio of Cu^+ with 86.1% compared with that of Cu–O_4(Ti) with 67.9%, signifying the low valence state of surface Cu. In contrast, Ti $2p_{3/2}$ and $2p_{1/2}$ peaks showed a slight blue-shift (~0.13 eV) post orbital engineering, suggesting an electron outflow at interfacial Ti sites (Supplementary Fig. 9b)[45]. Taken together, a strong *d*–*d* coupling may appear in Cu–Ti_1O_3, which modulates the local electron density distribution and results in *l*-Cu sites[46]. Moreover, the structures of these two catalysts were also studied by Raman spectroscopy (Supplementary Fig. 11). The bands at 637, 517, 395, 200, and 146 cm^{-1}

were observed for all of Cu SACs and TiO_2, which could be ascribed to the vibrational mode of $E_{g(3)}$, A_{1g} & $B_{1g(2)}$, $B_{1g(1)}$, $E_{g(2)}$, and $E_{g(1)}$, respectively[45]. The $E_{g(1)}$ band in Cu–Ti_1O_3 showed the highest wavenumber among all samples, indicating the highest O_v concentration[45].

To further investigate the electronic states and coordination environment at Cu sites, X-ray absorption spectroscopy (XAS) was conducted at the Cu K-edge. X-ray absorption near-edge fine structure exhibited that the adsorption edges and corresponding first derivative peaks of two Cu SACs lay between those of Cu_2O and CuO references (Fig. 3d and Supplementary Fig. 12), suggesting the existence of major $Cu^{\delta+}$ species in Cu SACs. The peak position of Cu–Ti_1O_3 catalyst (8982.3 eV) was lower than Cu–O_4(Ti) catalyst (8982.7 eV, Supplementary Fig. 12), further indicating localized electronic states of *l*-Cu sites when O_v accumulation, consistent with the results of XPS. As for extended X-ray absorption fine structure (EXAFS) spectra, the Fourier-transformed EXAFS exhibited an intense peak at R ≈ 1.92 Å for Cu–O_4(Ti) (Fig. 3e and Supplementary Fig. 13; Supplementary Table 4), which may be ascribed to Cu–O bonds[15]. While the wavelet-transformation analyses revealed the absence of Cu–Cu bonds in Cu–O_4(Ti), confirming the formation of Cu–O–Ti motifs where an average Cu–Ti interatomic distance of 2.97 Å was observed (Supplementary Fig. 14)[16]. While in Cu–Ti_1O_3, a peak at $R = 2.83$ Å appeared, and wavelet-transformed EXAFS revealed a high-energy region at ~6.53 $Å^{-1}$ (Supplementary Fig. 14), which together confirms the formation of Cu–Ti bonds[46]. The generation of Cu–Ti bonds, originating from O_v accumulation, implies a strong *d*–*d* orbital coupling in Cu–Ti_1O_3.

Electrochemical measurements

The catalytic performance of CO_2RR was then tested in a flow cell with 1 M KOH electrolyte (Details in "Methods"). The linear sweep voltammetry curves with the CO_2 flow revealed a higher reaction current for Cu–Ti_1O_3 than Cu–O_4(Ti) (Supplementary Fig. 15). in situ electrochemical impedance spectroscopies (EIS) at −0.88 V were executed, which showed that Cu–Ti_1O_3 obtained lower charge-transfer resistance compared with Cu–O_4(Ti) (Supplementary Fig. 16 and Table 5). Corresponding advanced distributed relaxation times analyses exhibited two characteristic peaks at −0.88 V over two catalysts, i.e., P2 and P3, which refer to the charge-transfer process of CO_2RR and HER, respectively[47]. The interfacial charge transfer impedances of CO_2RR on Cu–Ti_1O_3 were calculated as 48.62 Ω, lower than that over Cu–O_4(Ti) (123.7 Ω), while the trend was opposite toward HER (Supplementary Table 6), indicating a more favorable CO_2RR pathway on Cu–Ti_1O_3.

In electrolysis experiments, Cu–Ti_1O_3 achieved a peak FE_{CH_4} of 76% at −0.88 V, about 2.2-fold higher than Cu–O_4(Ti) (Fig. 4a and Supplementary Fig. 17). The FE ratios of CH_4 to $2e^-$-product (CO + HCOOH) were calculated as 14.2 on Cu–Ti_1O_3, much larger than that of Cu–O_4(Ti) (Fig. 4b and Supplementary Fig. 18), indicating a favorable multi-electron (>$2e^-$) pathway on Cu–Ti_1O_3. Furthermore, partial current density of CH_4 (J_{CH_4}) on the Cu–Ti_1O_3 reached a maximal value of 670 mA cm^{-2} at −1.00 V (i.e., turnover frequency of CH_4 (TOF_{CH_4}) = 24,930 h^{-1}, Fig. 4c), surpassing Cu–O_4(Ti) (J_{CH_4} = 205 mA cm^{-2}, TOF_{CH_4} = 7100 h^{-1}). The corresponding J_{CH_4} normalized by electrochemically active surface area (ECSA) was also calculated to eliminate the influence of the reaction surface, and Cu–Ti_1O_3 delivered a 2.5 times greater current density than Cu–O_4(Ti) (Supplementary Fig. 19). Furthermore, the energy efficiency (EE) of Cu–Ti_1O_3 attained a peak value of 38.7% at −0.88 V, exceeding that on Cu–O_4(Ti) (19.2%, Fig. 4d). By tuning the CO_2 flow rate to 50 sccm, the Cu–Ti_1O_3 achieved the largest FE_{CH_4} of 79% at around −0.88 V, while the peak FE_{CH_4} of the Cu–O_4(Ti) was 38% (Supplementary Fig. 20). The pristine TiO_2 showed that H_2 was dominant product (FE > 95%) with no detection of carbonous product, confirming that Cu sites on the support facilitate the CO_2RR (Supplementary Fig. 21). For mechanistic insight, O_v-free Cu_1/MgO(Al) without other *d*-block elements was then synthesized and tested (Details in Supplementary Note 2, XRD/XPS/TEM/EDS in Supplementary Figs. 22 and 23), exhibiting a FE_{CH_4} of less than 30% (Supplementary Fig. 24), further suggesting the essential role of O_v-intensified *d*–*d* orbital coupling. We then study the influence of impurities such as sulfur dioxide (SO_2) and oxygen (O_2) on the CO_2RR performance of Cu–Ti_1O_3 at −0.88 V. Under pure CO_2 flow, the Cu–Ti_1O_3 realized a high FE_{CH_4} of ~76%. However, upon introducing 1% SO_2 (~10^4 ppm) at $t = 0.5$ h, the total FE, along with FE_{CH_4}, decreased markedly (Supplementary Fig. 25a), which can be attributed to the preferential reduction of SO_2[48]. After 1 h of electrolysis (including a feed of 1% SO_2 for 30 min), the FE_{CH_4} recovered to >66%, suggesting that the influence of SO_2 on the catalyst structure is largely reversible. A similar reversible trend was observed when feeding 10% O_2 (~10^5 ppm, Supplementary Fig. 25b).

Both two catalysts were further integrated into a 5-cm^2 zero-gap electrolyzer to evaluate the potential of our strategies for practical applications towards the CH_4 formation (Supplementary Fig. 26). The Cu–Ti_1O_3 exhibited a higher FE_{CH_4} of 75% than that of Cu–O_4(Ti) (37%) at a constant current density of −0.6 A cm^{-2} (Supplementary Fig. 27). Catalyst stability was then evaluated at −0.6 A cm^{-2}. Cu–Ti_1O_3 maintained continuous operation for >1230 h at an industrial current density of −0.6 A cm^{-2}, exhibiting a cell voltage of −4.05 ± 0.16 V and an average FE_{CH_4} of ~71% (Fig. 4e). Post-test XRD, HRTEM, aberration-corrected HAADF-STEM, and XPS confirmed structural integrity via persistent *d*–*d* coupling (Supplementary Figs. 28–32). In contrast, Cu–O_4(Ti) showed rapid degradation: FE_{CH_4} dropped to 23% within 64 h under identical conditions, with observed Cu nanoparticle formation that suggests Cu–O bond cleavage and metallic atomic aggregation. In addition, the Cu content of Cu–Ti_1O_3 after reaction was almost unchanged, yielding less Cu dissolution (5 ppb vs. 65 ppb for Cu–O_4(Ti), Supplementary Tables 7 and 8), implying screened Cu corrosion. From the perspective of reaction activity and stability, Cu–Ti_1O_3 surpassed most of the advanced Cu SACs in CH_4 production metrics (Fig. 4f and Supplementary Table 9). Moreover, techno-economic assessments based on a power plant model (Details in Supplementary Note 3 and Supplementary Fig. 33), utilizing established literature parameters[21,49] and the durability data presented herein (Supplementary Table 10), demonstrate that a profitable pathway is feasible for this CO_2-to-CH_4 conversion system under a given carbon price (Supplementary Fig. 34).

Mechanism investigations

To gain insight into the role of orbital engineering in modulating the reaction mechanism, a series of in situ electrochemical spectroscopies was employed. In situ time-field E-EMR tracked O_v dynamics and intermediates during CO_2RR. For Cu–Ti_1O_3, the time-field scans suggested that a signal related to O_v (centered at *g*-tensor of 1.997) maintained well after 10-min CO_2 injection, excluding the influence of CO_2 adsorption on the O_v concentrations (Fig. 5a and Supplementary Fig. 35). However, O_v gradually faded out under applied potential, and recovered when the potential was revoked (Fig. 5a). On the contrary, Cu–O_4(Ti) catalyst exhibited a maintained O_v intensity throughout the catalytic process (Supplementary Fig. 36). Further quantitative spin counting (Fig. 5b) showed an initial O_v concentration of 1.08×10^{17} spins in Cu–Ti_1O_3, approximately 3 times higher than that in Cu–O_4(Ti) (3.52×10^{16} spins). Under applied potential, O_v concentration of Cu–Ti_1O_3 dropped to 3.78×10^{16} spins, while recovering to 1.08×10^{17} spins at open-circuit potential (OCP), suggesting an intermediate-mediated (e.g., $*OCH_3$) reversible O_v occupancy process. We then used heavier deuterium (D) from D_2O solvent as the source of H to investigate the O_v concentration variation during CO_2RR. Under applied potential, O_v concentration decreased to 5.81×10^{16} spins, higher than that using H_2O as solvent under the same condition (Supplementary Fig. 37). As hydrogenation activity is weakened in D_2O[50], lower $*OCD_3$ was produced during CO_2RR, hence causing a lower occupancy rate of

https://doi.org/10.1038/s41467-026-69260-z

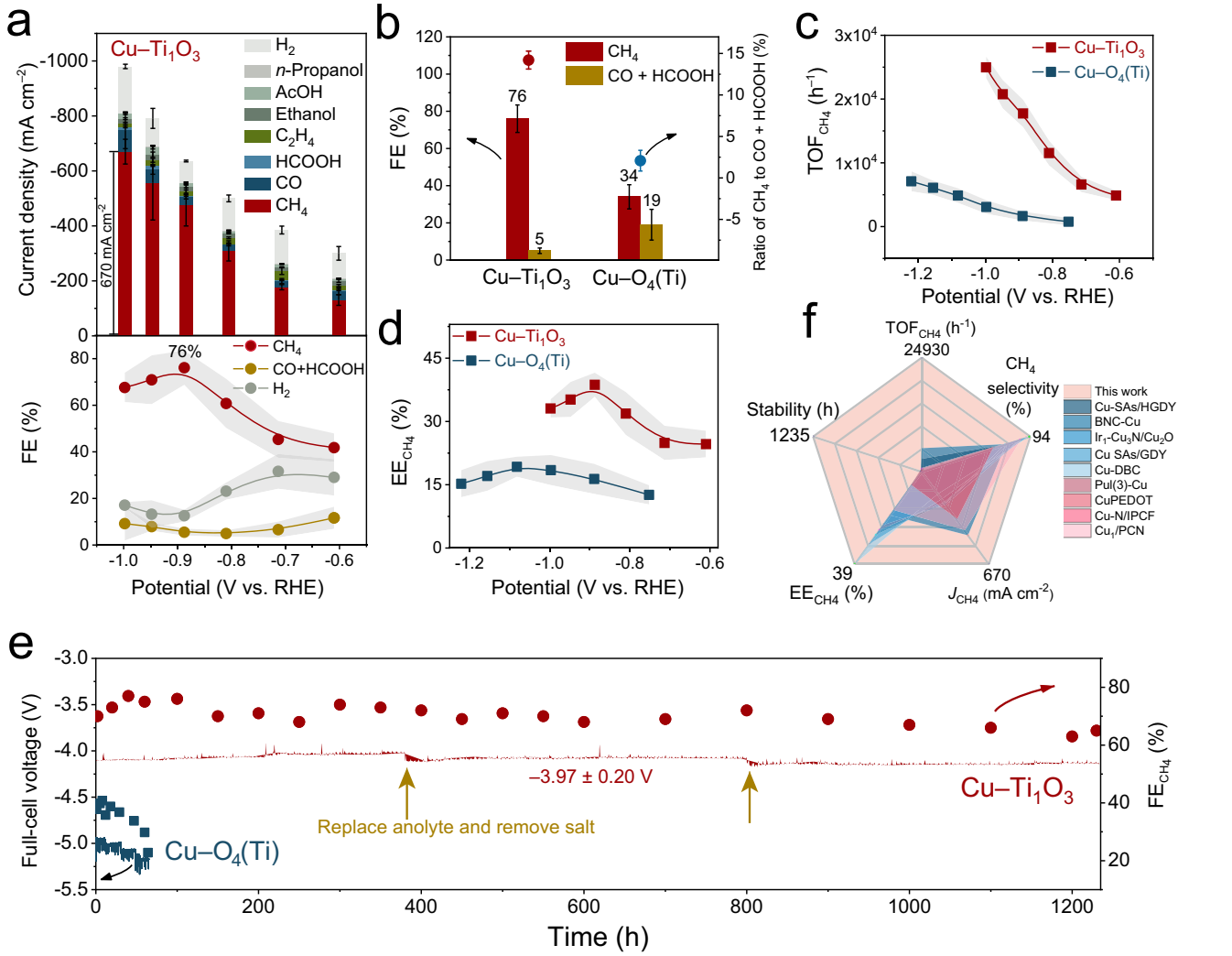

Fig. 4 | Electrocatalytic performance over different catalysts. a Current densities (top) and FEs (bottom) of CO_2RR product and H_2 on Cu–Ti_1O_3 catalyst at different applied potentials in 1 M KOH (with 90% *iR*-correction). **b** FEs and corresponding ratios of CH_4: (HCOOH + CO) on Cu–Ti_1O_3 and Cu–O_4(Ti) at around −0.88 V. **c** TOFs of CH_4 on Cu–Ti_1O_3 and Cu–O_4(Ti) catalysts at different applied potentials (with 90% *iR*-correction). **d** Energy efficiency (EE) of CH_4 on Cu–Ti_1O_3 and Cu–O_4(Ti) catalysts (with 90% *iR*-correction). Cell resistance and pH of 1 M KOH electrolyte were measured as 0.98 ± 0.06 Ω and 14.00 ± 0.02, respectively, with an electrode surface area of 1 cm^2. **e** Stability tests in a 5-cm^2 zero-gap electrolyzer with 0.1 M $KHCO_3$. **f** Comparison of this work with state-of-the-art CO_2RR electrocatalysts, including J_{CH_4}, CH_4 selectivity, EE_{CH_4}, stability and TOF_{CH_4}. Data are presented as mean ± s.d. (n = 3), with the error bars representing the s.d. Source data for Fig. 4 are provided as a Source Data file.

O_v. To reveal these short-lived intermediates, the spin traps were spiked under flow employing 5,5-dimethyl-1-pyrroline N-oxide (DMPO)[51] (Supplementary Fig. 38). A typical six-finger peak (g = 2.0055, A_N = 1.35 mT, $A_{H\beta}$ = 0.74 mT) appeared (Fig. 5c), exhibiting a negative correlation with O_v, which demonstrated the replacement of O_v by alkoxy (i.e., *OCH_3). Subsequently, this signal disappeared during the power outage, and signals associated with O_v gradually reverted to their initial state. The O_v concentration of Cu–Ti_1O_3 was also probed during water electrolysis, which retained well, indicating that H_2O and *OH adsorption have only a minor influence on O_v stability (Supplementary Fig. 39). Signal reversibility during potential interruption confirmed O_v's dynamic participation in CO_2RR on Cu–Ti_1O_3, revealing a new *OCH_3 insertion mechanism (Supplementary Fig. 40). Notably, as methoxyl radicals (*OCH_3) are typically poorly detectable in bulk water solution, this result is more indicative of an association with the electrochemical interface. By regulating the calcination condition, the O_v concentration could be controlled rationally (Supplementary Fig. 41). EMR spectra showed that the O_v concentration of catalyst increased to higher values with 1.58×10^{17} spins when calcined in 10% H_2/Ar for 4 h, which could further improve the FE_{CH_4} to 78%. However, the TOF_{CH_4} per O_v of Cu–Ti_1O_3 showed the maximum value with 1.62×10^{-13} h^{-1} $spin^{-1}$ (Supplementary Fig. 41e), indicating the most efficient CH_4 formation on *l*-Cu sites.

The quasi-operando XPS also revealed the dynamic switch of O_v during CO_2RR from a semi-quantitative perspective. For Cu–Ti_1O_3, O_v content decreased to 15.9% after 10-min electrolysis (intermediate-retained state), while recovering upon degassing (Supplementary Fig. 42a). This reversible change indicates pseudo-lattice oxygen formation by adsorbed intermediates. Concurrent Ti 2*p* binding energy upshift correlated with O_v depletion (Supplementary Fig. 42b), further evidencing intermediate-induced electronic perturbation. In stark contrast, Cu–O_4(Ti) showed negligible O_v/Ti 2*p* changes (Supplementary Fig. 42c, d), confirming Cu–O–Ti motifs' minimal reactivity impact. Complementary in-situ Raman (Supplementary Fig. 43) also revealed a reversible downshift of the $E_{g(1)}$ band (147→143 cm^{-1}) in Cu–Ti_1O_3 during reaction (Fig. 5d), while remaining invariant in Cu–O_4(Ti) (Fig. 5e), consistent with the *OCH_3 insertion mechanism mentioned above. These results elucidate the unique mechanistic pathway governing CH_4 formation on Cu–Ti_1O_3, mediated through *d*–*d* orbital coupling at *l*-Cu sites.

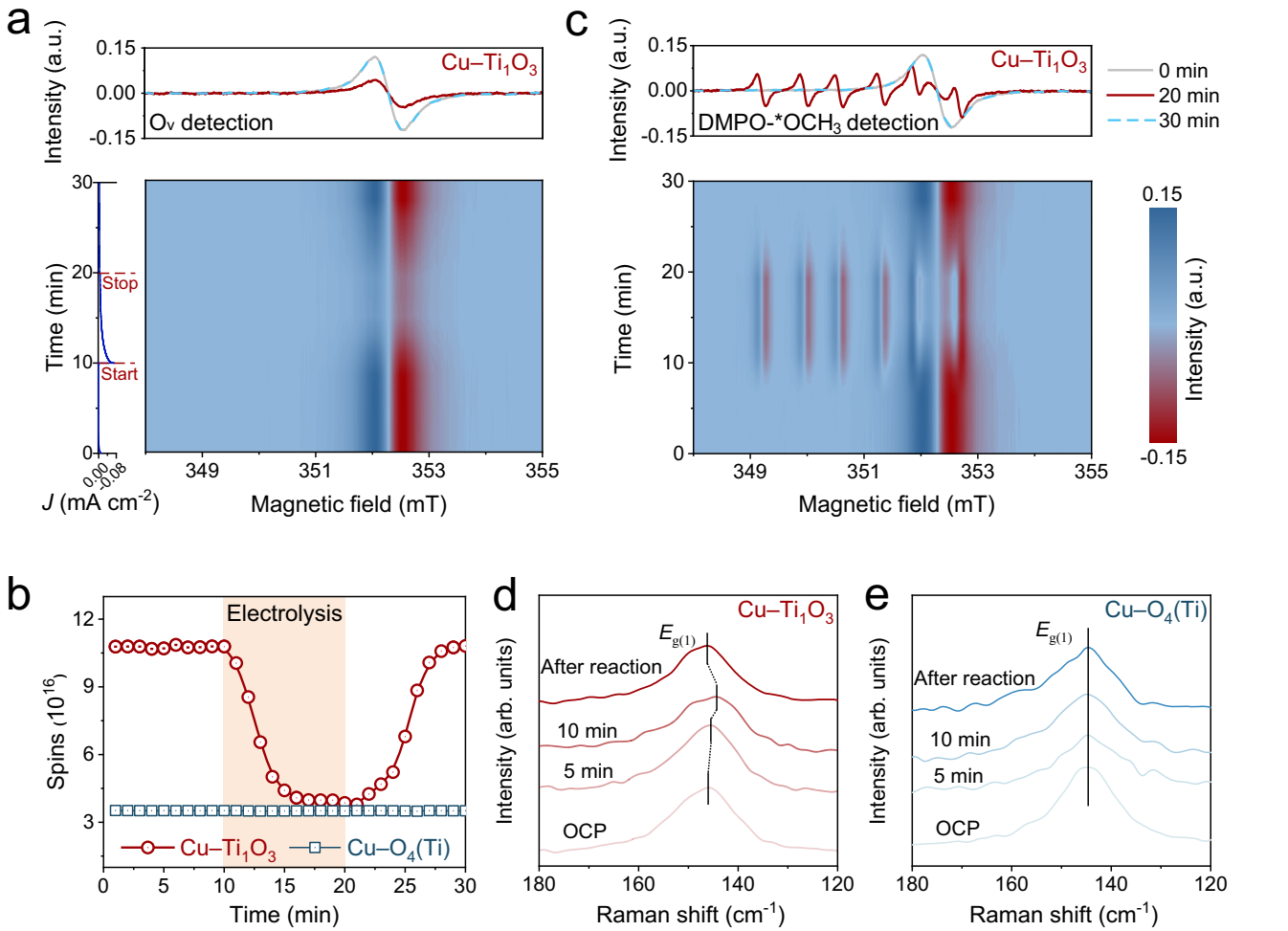

Fig. 5 | In-situ electrochemical spectra measurements. a In-situ time-field E-EMR spectra in CO_2-saturated 0.1 M $KHCO_3$ at −0.88 V over Cu−Ti_1O_3 (with 90% *iR*-correction), referring to in-situ O_v evaluation. **b** Quantitative spin counts of signals related to O_v versus time over Cu−Ti_1O_3 and Cu−O_4(Ti). **c** In-situ time-field E-EMR spectra with spin-trap agent (i.e., DMPO) in CO_2-saturated 0.1 M $KHCO_3$ at −0.88 V over Cu−Ti_1O_3 (with 90% *iR*-correction), corresponding to the in-situ concentration assessments for both O_v and $*OCH_3$ intermediate during CO_2RR. **d** In-situ Raman spectra of Cu−Ti_1O_3 and **e** Cu−O_4(Ti) during a 10-min CO_2RR in CO_2-saturated 0.1 M $KHCO_3$ at −0.88 V (with 90% *iR*-correction). Cell resistance and pH of electrolyte were measured as 0.98 ± 0.06 Ω and 6.83 ± 0.03, respectively, with an electrode surface area of 1 cm^2. Source data for Fig. 5 are provided as a Source Data file.

CO_2 temperature-programmed desorption (CO_2-TPD) was then carried out to assess the CO_2 adsorption capacity of the Cu SACs (Supplementary Fig. 44). Cu−Ti_1O_3 displayed a large chemisorption peak at a higher temperature (455 °C), compared with the weak chemisorption peak of Cu−O_4(Ti) at 430 °C, manifesting the intensive CO_2 adsorption ability[52]. In situ attenuated total reflection surface-enhanced infrared absorption spectroscopy (ATR-SEIRAS, Supplementary Fig. 45) was then employed to probe intermediates. On Cu−Ti_1O_3, the 1355 cm^{-1} peak (i.e., *COOH)[12] at −0.1 V disappeared distinctly at −0.5 V, indicating rapid conversion to *CO (Fig. 6a). Both catalysts exhibited linear-bonded *CO ($*CO_L$) at ~2075 cm^{-1} (Fig. 6a, b)[53,54], with Cu−Ti_1O_3 showing stronger intensity over wider potentials, reflecting higher *CO coverages. CO_L signal on Cu−O_4(Ti) red-shifted with increasing applied potential, ascribing to the Stark effect[55]. In contrast, CO_L peak on Cu−Ti_1O_3 intensified and blue-shifted with the potential increasing to −1.1 V. This phenomenon is ascribed to dipole–dipole coupling resulting from the increased *CO coverage at localized $Cu^{\delta+}$ sites and adjacent Ti atom[55,56]. The in-situ ATR-SEIRAS spectra of pristine Au film, which served as the SEIRAS-active template, were also measured during CO_2RR (Supplementary Fig. 46). A peak observed at ~2100 cm^{-1} was assigned to adsorbed *CO[57], confirming that the detected $*CO_L$ peak on the Cu−Ti_1O_3 surface indeed stems from Cu−*CO interaction. The in-situ Raman spectra showed a band at around 358 cm^{-1} (Supplementary Fig. 47), which was attributed to the frustrated rotation of adsorbed *CO on Cu[58]. A distinct *CO signal at low cathodic potential further highlights the higher *CO coverage on Cu−Ti_1O_3 surface. Moreover, C−H bending modes of $*OCH_3$ appeared[53], yet notably red-shifted on Cu−Ti_1O_3 (1380 cm^{-1}) versus Cu−O_4(Ti) (1398 cm^{-1}). This 18 cm^{-1} shift signifies reduced C−H vibrational frequency, consistent with stabilized $*OCH_3$ insertion at O_v mentioned above[35,59]. Meanwhile, earlier emergence and intensified $*OCH_3$ signal on Cu−Ti_1O_3 further evidence facilitated *CO hydrogenation toward CH_4.

DFT calculations were then carried out to assess the effect of orbital engineering on catalytic performance (Model details in Supplementary Data 1). The CO_2 adsorption features were first evaluated (Supplementary Table 11), and detailed charge density difference (CDD) analyses revealed an enhanced electron donation from Cu sites to $*CO_2$ on Cu−Ti_1O_3 (Fig. 6c). The highest CDD value on Cu−Ti_1O_3 was calculated as -1.8×10^{-3} e $Bohr^{-3}$ (63.6% larger than that on Cu−O_4(Ti)), showing a negative charge cloud (blue color in Fig. 6c) surrounded $*CO_2$, indicating a stronger *d*-π* polar-interaction. Moreover, the free energy diagrams illustrate how the CO_2RR pathways proceed on Cu single-atom sites (Fig. 6d). The overall free energy change (ΔG) for methanation (i.e., $*CO_2 \rightarrow * + H_2O_{(l)} + CH_{4(g)}$) on both Cu SACs shows energy downhill, indicating a thermodynamically favorable

https://doi.org/10.1038/s41467-026-69260-z

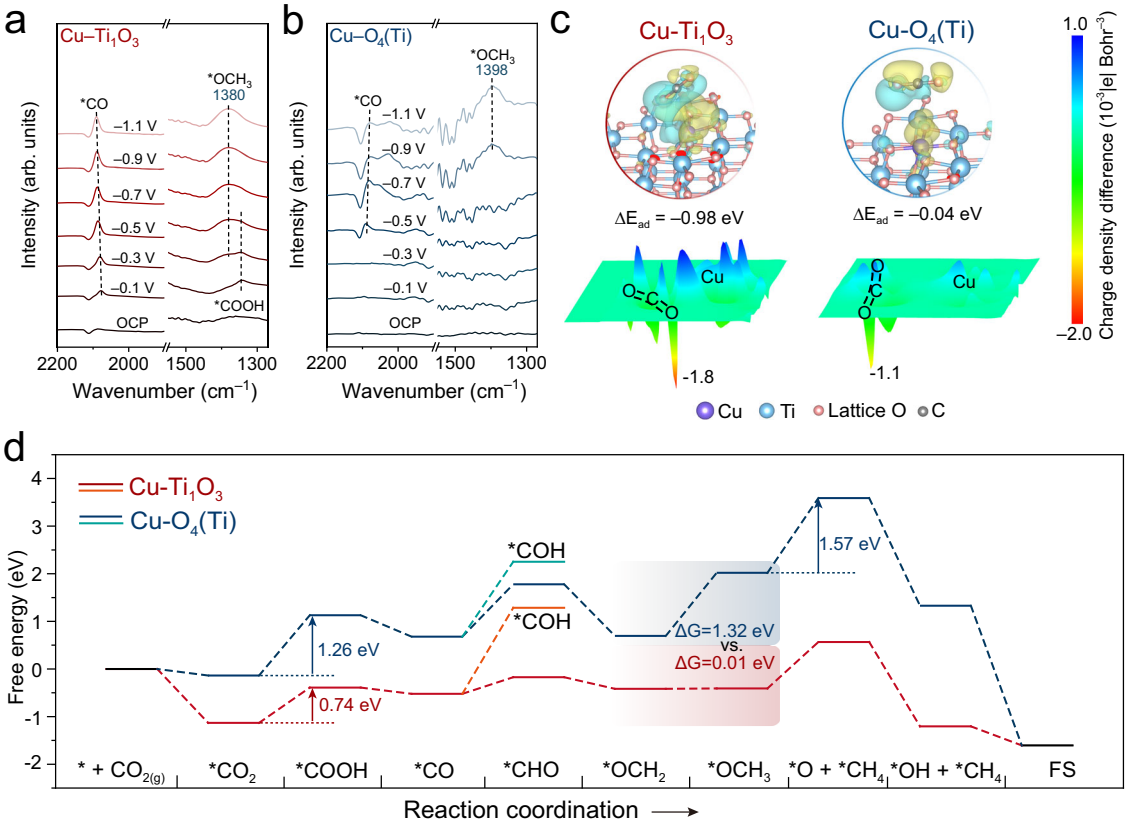

Fig. 6 | Mechanism research of CO_2RR on Cu single-atom catalysts. In-situ ATR-SEIRAS spectra on **a** Cu–Ti_1O_3 and **b** Cu–O_4(Ti) in a potential window from OCP to −1.1 V in CO_2-saturated 0.1 M $KHCO_3$ (with 90% *iR*-correction). Cell resistance and pH of electrolyte were measured as 0.98 ± 0.06 Ω and 6.83 ± 0.03, respectively, with an electrode surface area of 1 cm^2. **c** The charge density difference analyses of *CO_2 on Cu–Ti_1O_3 and Cu–O_4(Ti). Green isosurfaces indicate negative-charged regions, and the yellow isosurfaces refer to positive-charged regions when CO_2 is adsorbed on catalysts. **d** Free energy diagram of CO_2-to-CH_4 conversion on Cu–Ti_1O_3 and Cu–O_4(Ti) at 298.15 K. Source data for Fig. 6a, b, d are provided as a Source Data file.

methanation. With the Brønsted–Evans–Polanyi relation, we further assessed the reaction kinetics in CO_2-to-CH_4 conversion. For *CO_2→*COOH conversion, Cu–Ti_1O_3 displayed a 0.52 eV smaller energy rise relative to Cu–O_4(Ti), suggesting a promoted CO_2 activation resulting from stronger *d*-π* polar-interactions[36,37], which has been mentioned in Fig. 2b. For the vital *OCH_3 intermediate, ΔG for *OCH_2→*OCH_3 step was only 0.01 eV on Cu–Ti_1O_3, ~100% reduction from that on Cu–O_4(Ti), demonstrating the accelerated kinetics induced by the new *OCH_3 insertion mechanism at *l*-Cu sites. Meanwhile, ΔG for hydrogenation of *OCH_3 was 1.57 eV and 0.97 eV on Cu–O_4(Ti) and Cu–Ti_1O_3, respectively (Fig. 6d), revealing faster *OCH_3-to-*CH_4 converting kinetics at *l*-Cu sites. Taken together, the DFT calculations indicate a more favorable CO_2-to-CH_4 conversion on Cu–Ti_1O_3, which is attributed to the localization of Cu electronic states and subsequently enhanced *d*-π* polar-interaction and Cu–O bonding.

Discussion

In summary, we employed oxygen-vacancy-involved orbital engineering to construct localized Cu single-atom sites on O_v-rich TiO_2 toward efficient methanation. Oxygen vacancies intensify *d*–*d* orbital coupling between Cu and Ti, heightening the electronic localization at *l*-Cu sites. This coupling strengthens the *d*-π* polar-interaction on *CO_2, and helps switch the O in *OCH_3 to pseudo-lattice oxygen. These synergistic effects promote the CO_2 activation and targeted cleavage of the C–O bond in *OCH_3, thus driving efficient CH_4 production. In electrocatalytic experiments, Cu–Ti_1O_3 catalyst achieves a FE_{CH_4} of 76%, a peak TOF_{CH_4} of 24,390 h^{-1}, and record-long durability of >1230 h at industrial-level current densities. This work highlights the prospect of *d*-orbital engineering in enabling industrial-level electrocatalytic methanation on Cu SACs, and provides a promising catalyst design strategy toward sustainable CH_4 production for decarbonizing traditional thermal power plants.

Methods

Chemicals and materials

Potassium hydroxide (KOH, ≥85.0%), Sodium hydroxide (NaOH, ≥85.0%), acetone (99.7%), ethanol (99.7%), glycerol (99.7%), Copper chloride dihydrate ($CuCl_2{\cdot}2H_2O$, ≥99.0%), Titanium oxysulfate dihydrate ($TiOSO_4{\cdot}2H_2O$, ≥99.0%), Magnesium nitrate hexahydrate ($Mg(NO_3)_2{\cdot}2H_2O$, ≥99.0%) and Aluminum nitrate nonahydrate ($Al(NO_3)_3{\cdot}9H_2O$, ≥99.0%) were purchased from the Sinopharm Chemical Reagent Company. Ni foam was purchased from the Fangdou Technology Co., LTD (99% metal basis) with 0.3 mm thickness and 0.1 mm pore size. The Nafion solution (Dupont, D-520 dispersion, 5% w/w in water and 1-propanol) and triethylene glycol were purchased from Alfa Aesar. Gas diffusion layer (SGL Carbon, 28BC) was purchased from Fuel Cell Store. The hydroxide exchange membrane (Fumasep FAB-PK-130, 3 × 2 cm) for the flow cell was purchased from Fumatech, which was activated by soaking in 1 M KOH for 24 h for further test. The hydroxide exchange membrane (Grade 60, 3 × 3 cm) for the zero-gap electrolyzer was purchased from Dioxide Materials, which was activated by soaking in 1 M KOH for 24 h before the test. CO_2 gas (99.99%), Ar gas (99.99%), N_2 gas (99.99%), and all the standard gases were purchased from Shanghai Tomoe Gas Company.

Fabrication of Cu–Ti1O3

In a typical procedure, 2.2 g $TiOSO_4{\cdot}2H_2O$, 0.15 g $CuCl_2{\cdot}2H_2O$, 12 mL deionized water, 6 mL glycerol, and 20 mL ethanol were mixed and

stirred for 1 h. The mixed solution was then moved into a 100 mL autoclave and kept at 200 °C for 8 h, followed by natural cooling to room temperature. Finally, the precipitate was washed thoroughly with alcohol and dried at 60 °C in a vacuum oven overnight. The sample was then calcined at 300 °C in 10% H_2/Ar for 3 h to obtain the Cu–Ti_1O_3 catalyst.

Fabrication of Cu–O4(Ti)

Cu–O_4(Ti) were prepared in a similar way as Cu–Ti_1O_3 nanoparticles, except that the final sample was calcined at 300 °C in the air for 3 h.

Preparation of electrodes

For the CO_2RR in a flow cell, a well-dispersed catalyst slurry containing 18 mg of catalysts, 3 mL of acetone, and 120 µL of Nafion (Dupont, D-520 dispersion, 5% w/w in water and 1-propanol) ionomer solution was slowly dropped onto a gas diffusion layer (SGL Carbon, 28BC), attaining a catalyst loading of ~0.3 mg cm^{-2} measured by 0.01 mg analytical balance.

Materials characterizations

XRD was tested on a Bruker SMART APEX (II)-CCD. XPS data were characterized by a Thermo Scientific K-Alpha XPS. Scanning electron microscopy measurements were carried out by a Hitachi S4800 SEM. HRTEM measurements were performed by a JEM 2100 F (JEOL, Japan). ^{1}H-nuclear magnetic resonance (^{1}H-NMR) measurements were performed on a Bruker AVANCE AV III HD 500. Moreover, Athena and Artemis software with a standard IFEFFIT package were used to process XAS data.

Electrocatalytic CO2 reduction measurements

For CO_2RR in flow-cells, the electrochemical tests were conducted using a 1-cm^2 cell with a Gamry (Model: Reference 3000) electrochemical workstation at room temperature (25 ± 1 °C). The flow-cell configuration consists of a gas diffusion layer loaded with catalysts as the working electrode, a Ni foam as the anode, an Ag/AgCl electrode as the reference, and an anion exchange membrane to separate the cathode and anode chambers (Supplementary Fig. 48). The chamber volume of the cathode and anode is 0.5 cm^3. All applied potentials were converted to the RHE scale according to the Nernst equation:

$$E_{RHE} = E_{Ag/AgCl^0} + 0.197 + 0.059 \times pH \quad (1)$$

The electrode potential was *iR*-corrected using the following equation:

$$E_{sample} = E_{applied} - 0.9 \times I_{total} \times R_{cell} \quad (2)$$

where E_{sample} was the corrected potential at the cathode, $E_{applied}$ was the applied potential, and I_{total} was the total current. R_{cell} was the cell resistance of 0.98 ± 0.06 Ω, which was measured via potentiostatic EIS.

1 M KOH solution (pH = 14.00 ± 0.02) was utilized as the electrolyte that was prepared before electrochemical tests to ensure freshness. The reaction was performed with a steady stream of CO_2 (30 mL min^{-1}) measured by a soap bubble flowmeter. The gas product was collected and analyzed by a gas chromatograph (Shanghai Ramiin GC 2060) while the liquid products were quantified by ^{1}H-NMR spectroscopy (Bruker AVANCE AV III HD 500) using a method previously reported[60].

The gas product FE was calculated by the following equation:

$$FE(\%) = N \times F \times \frac{S_x}{S} \times C \times \upsilon / I \times 100\% \quad (3)$$

where *N* was the number of charge transfers (H_2: 2; CH_4: 6; C_2H_4: 8); S_x was the peak area of the gas product and *S* was the peak area of corresponding standard gas; *C* was the concentration of standard gas; υ was the flow rate of CO_2; *I* was the real-time current during CORR; *F* was the Faraday constant (96485 C mol^{-1}).

The liquid product FE was calculated by the following equation:

$$FE(\%) = N \times V \times C \times F / Q \times 100\% \quad (4)$$

where *N* was the number of charge transfers (Acetate: 4; EtOH: 8; *n*-PrOH: 12); *V* was the electrolyte volume (20 mL); *C* was the concentration of products; *Q* was the reaction charge.

The ECSA was calculated by assuming a monolayer of Pb adatoms over a Cu surface and 2e^- Pb oxidation with a conversion factor of 310 µC cm^{-2} [61]. The EIS was performed at an open-circuit potential state in the frequency range from 100 kHz to 100 MHz. The Pb underpotential deposition was conducted in an Ar-saturated 0.1 M $HClO_4$ aqueous solution with 10 mM $Pb(ClO_4)_2$ by using cyclic voltammetry. This is the deposition of an adlayer of a foreign metal (i.e., Pb^{2+}) on a substrate (i.e., surface Cu site) at potentials higher than the thermodynamic reduction potential of the electrodeposited metal. The foreign metal tends to deposit on the Cu rather than TiO_2 due to higher electrical conductivity, leading to accurate deposition on the Cu surface[62]. Before the experiment, the potential was first set at −0.20 V vs. RHE for 150 s, then swept from −0.0840 to 0.161 V vs. RHE with a sweep rate of 10 mV s^{-1}.

Stability tests in a zero-gap electrolyzer

The zero-gap electrolyzer (Shanghai Keqi, active area 5 cm^2, Supplementary Fig. 26) was utilized, which was established with a well-established membrane electrode assembly containing a cathode electrode, an anion membrane (Dioxide Materials, Grade 60), and an anode electrode (Ti mesh loaded with 2 mg cm^{-2} IrO_x). 0.05 M HCl-humidified CO_2 was supplied with a flow rate of 30 sccm through the flow channels in the cathode flow field to reduce (bi)carbonate salt accumulation according to previous work[63], and 0.1 M $KHCO_3$ (pH = 6.83 ± 0.03) was fed into the anode flow channels with a flow rate of 15 sccm. The stability tests were performed at a constant current of −3 A. During operation, the anolyte was replaced regularly, and the precipitated salt was further removed by separating the device to inhibit channel block and active site shield.

Calculation for EE

For flow-cell systems, the EE_{CH_4} was calculated based on the assumption that the overpotential of oxygen evolution is zero. The methane EE_{CH_4} can be calculated as follows:

$$EE_{CH_4} = \frac{(1.23 + (-E_{CH_4})) \times FE_{CH_4}}{(1.23 + (-E_{applied}))} \quad (5)$$

where $E_{applied}$ is the potential applied in the experiment, FE_{CH_4} is the measured FE of CH_4 in percentage, and E_{CH_4} = 0.17 V vs. RHE for CO_2RR[64].

For the zero-gap electrolyzer, EE_{CH_4} is calculated as follows:

$$EE_{CH_4} = \frac{(1.23 + (-E_{CH_4})) \times FE_{CH_4}}{-E_{full-cellapplied}} \quad (6)$$

where $E_{full\text{-}cell\ applied}$ is the full-cell voltage applied in the zero-gap electrolyzer.

Calculation for TOF

The TOF of CH_4 is calculated according to the following equation:

$$TOF(h^{-1}) = \frac{I_{CH_4}/nF}{\alpha m_{cat.}/M_{Cu}} \times 3600 \quad (7)$$

Where n is the number of electrons transferred to CH_4 with 8, F is the Faradaic constant with 96485 C mol^{-1}, $m_{cat.}$ is the catalyst mass in the electrode, α is the mass ratio of surface Cu active sites in the catalyst measured by XPS, and M_{Cu} is the atomic mass of Cu.

In-situ electrochemical electron magnetic resonance

The in-situ E-EMR was carried out on a self-made in-situ cell according to our previous report with the employment of a magnetic resonance spectrometer (CIQTEK, EPR200, China)[65]. The 0.17 M of DMPO (Dojindo Laboratories, Japan) was selected as the trap agent without additional purification. In the Schlenk line, the just-prepared electrode was cleaned in argon and then pumped with CO_2. The electrochemical analyzer (CHI852D, CH Instrument, USA) applied multi-step potentials and recorded current response with sequential 10 min of 0, −0.88, and 0 V vs. RHE. The collaboration between magnetic resonance and electro-analysis was ensured through a serial communication port. The obtained raw data were processed and analyzed based on Easyspin 6.0.6[66,67].

In-situ electrochemical infrared spectroscopy experiments

The in-situ attenuated total reflection surface enhanced infrared absorption (ATR-SEIRAS) measurements were conducted on a home-made spectro-electrochemical cell (Supplementary Fig. 31). A ~60-nm-thick SEIRA-active Au film was pre-deposited on the reflection plane of a semicircular cylinder Si prism. Then, the catalyst was drop-cast on the above film. The operando ATR-SEIRAS measurements were performed in an optical system embedded in the spectroscopic chamber. To reach a high signal/noise ratio, the spectrum was obtained by averaging 256 interferograms. The incident angle of the IR beam was set to 55°. The spectra were shown as absorbance defined as $A = -\log I_1/I_2$, where I_1 and I_2 represent the irradiation intensity of incident and reflective beams, respectively.

For nano Au film preparation, a hemicylindrical Si prism was polished and then cleaned with the RCA method: soaking it in a 1:1:5 (v/v) solution of NH_3, H_2O_2, and H_2O, and afterward in a 1:1:5 (v/v) solution of HCl, H_2O_2, and H_2O at about 80 °C, followed by rinsing with water. Then the total reflecting plane was immersed in 40% NH_4F solution for 90 s to terminate the Si surface. Deposition of Au was performed at 60 °C by dropping a mixture of a plating solution and 2% HF (2:1 v/v) onto the Si surface, and the deposition time was 60 s. The composition of the plating solution was 0.015 M $NaAuCl_4{\cdot}2H_2O$ + 0.15 M Na_2SO_3 + 0.05 M $Na_2S_2O_3{\cdot}5H_2O$ + 0.05 M NH_4Cl. After deposition, the prism was rinsed with deionized water to finish the deposition.

For catalyst deposition, a well-dispersed catalyst slurry containing 18 mg of catalysts, 3 mL of acetone, and 120 μL of Nafion ionomer solution was slowly dropped onto Au film, attaining a catalyst loading of ~0.3 mg cm^{-2} that can cover the Au film.

In-situ Raman experiments

A Raman spectrometer (HORIBA Jobin Yvon Inc., Model: HR Evolution) coupled with an optical microscope was used for in-situ Raman spectroscopy. A near-infrared laser (λ = 532 nm) was used as the excitation source. The types of objective and grating were 50XL and 500 nm, respectively. A homemade spectro-electrochemical cell equipped with a Pt wire counter electrode and an Ag/AgCl reference electrode was used, with the working electrode prepared by coating the catalyst onto glassy carbon. Each potential was maintained for at least 10 min before collecting the spectra.

Quasi-in-situ XPS measurement

All samples were prepared in the glovebox with an oxygen concentration of less than 4 ppm. The samples were prepared through 10-min CO_2RR in Ar-saturated 1 M KOH at around −0.88 V, and were then packaged with liquid nitrogen protection to stabilize the surface reaction intermediate for studying its influence on O_v. For the exploration of the O_v structure after reaction over catalysts, the samples were prepared in the same reaction conditions and were then dried under vacuum at 120 °C for 24 h to remove the surface species.

Theoretical computational

DFT calculations were performed with the Vienna ab initio simulation package (VASP), and the detailed calculation methods and parameters are presented in Supplementary Note 4 and Supplementary Data 1. Generally, all structures were relaxed by a conjugate gradient method until the residual force component was <0.04 eV $Å^{-1}$, and the convergence criterion of total energy in the self-consistent field method was set to 10^{-6} eV. The original structure of anatase was employed for calculations with the parameters that $a = b = 3.7825$ Å, $c = 9.6150$ Å, and $\alpha = b = \gamma = 90.0000°$. With the relaxed cell structure, the (100) plane was utilized for further assessments according to XRD and TEM results. DFT + U calculations on the density of states were performed for both $Cu–Ti_1O_3$ and $Cu–O_4(Ti)$, and Lobster was employed for COHP analyses[68].

Furthermore, (100) surface was also employed for CO_2RR evaluations, using a slab model consisting of three atomic layers and 2 × 1-unit cells for the lateral dimensions, where the thickness of the vacuum was set at 12 Å to ensure that there was no superficial interaction between different layers. The total size for the established slab model was 7.6134 × 9.5168 × 21.3227 $Å^3$, and $\alpha = \beta = \gamma = 90.0000°$. The Brillouin zone of the supercell was sampled by a 3 × 3 × 1 uniform k-point mesh. All the energy calculations were based on a two-step process involving the structure relaxation in vacuum (i.e., electron energy, E_{DFT}) and a subsequent single-point calculation using an implicit solvation model.

The bond dissociation enthalpies of Cu−O and O−C in Cu−*O−CH_3 were calculated based on a similar method reported previously[15]:

$$\Delta H_{Cu-O} = H_{*+OCH_3} - H_{*OCH_3} \tag{8}$$

$$\Delta H_{O-C} = H_{*O+CH_3} - H_{*OCH_3} \tag{9}$$

where H_{*OCH_3} and H_{*O} are the enthalpies of the catalyst with adsorption of the corresponding molecules, H_{*O+CH_3} and H_{*O+CH_3} are the enthalpies of the corresponding bond-breaking models.

The Gibbs free energy change of formation (at T K) for each elementary step was calculated as:

$$\Delta G(T) = \Delta E_{DFT} + \Delta E_{sol} + \Delta G_{cor}(T) \tag{10}$$

where ΔE_{sol} was the solvation correction, $\Delta G_{cor}(T) = \Delta E_{ZPE} - T\Delta S + \Delta U(T)$ was obtained by processing frequency calculation results, and $\Delta G_{298.15K}$ was used to construct the free energy profiles. The computational hydrogen electrode model was also employed[69], in which the chemical potential of $(H^+ + e^-)$ is equal to that of half a H_2 molecule with a pH correction of $k_B T \ln([H^+])$.

Data availability

The data that support the findings of this study are available in the paper and its Supplementary Information. Source data are provided as a Source Data file. Source data are provided with this paper.

References

1. Guo, P. et al. Carbon dioxide emissions from global overseas coal-fired power plants. *Nat. Clim. Chang.* **14**, 1151–1157 (2024).
2. O'Brien, C. P. et al. CO_2 electrolyzers. *Chem. Rev.* **124**, 3648–3693 (2024).
3. Rakhsha, A. et al. Tandem gold/copper catalysis and morphological tuning via wrinkling to boost CO_2 electroreduction into C_{2+} products. *Nano Energy* **133**, 110457 (2025).

4. Stanley, J. S. et al. Sorbent-mediated electrocatalytic reduction of dilute CO_2 to methane. *J. Am. Chem. Soc.* **147**, 16099–16106 (2025).
5. Sun, Z. et al. Integrated CO_2 capture and methanation from the intermediate-temperature flue gas on dual functional hybrids of AMS/CaMgO||Ni_xCo_y. *Sep. Purif. Technol.* **307**, 122680 (2023).
6. Woldu, A. R. et al. Experimental and theoretical insights into single atoms, dual atoms, and sub-nanocluster catalysts for electrochemical CO_2 reduction (CO_2RR) to high-value products. *Adv. Mater.* **36**, 2414169 (2024).
7. Xu, Y. et al. Optimizing the selectivity of CH_4 electrosynthesis from CO_2 over cuprates through Cu—O bond length descriptor. *Angew. Chem. Int. Ed.* **64**, e202503745 (2025).
8. Yang, Q. et al. Ethylene electrosynthesis at low voltages enabled by dopant-induced modulation of the rate-determining step. *Nat. Synth.* **4**, 1396–1407 (2025).
9. Wu, M. et al. Emerging atomically precise metal nanoclusters and ultrasmall nanoparticles for efficient electrochemical energy catalysis: synthesis strategies and surface/interface engineering. *Electrochem. Energy Rev.* **7**, 10 (2024).
10. Santatiwongchai, J., Faungnawakij, K. & Hirunsit, P. Comprehensive mechanism of CO_2 electroreduction toward ethylene and ethanol: the solvent effect from explicit water–Cu(100) interface models. *ACS Catal.* **11**, 9688–9701 (2021).
11. Pérez-Rodríguez, S. et al. Single-atom Cu-N-C catalysts for the electro-reduction of CO_2 to CO assessed by rotating ring-disc electrode. *J. Energy Chem.* **88**, 169–182 (2024).
12. Dong, J. et al. Continuous electroproduction of formate via CO_2 reduction on local symmetry-broken single-atom catalysts. *Nat. Commun.* **14**, 6849 (2023).
13. Shen, W. et al. Self-healing Cu single-atom catalyst for high-performance electrocatalytic CO_2 methanation. *Nat. Commun.* **16**, 7943 (2025).
14. Cai, R. et al. The proximal protonation source in Cu-NH_x-C single-atom catalysts selectively boosts CO_2 to methane electroreduction. *Angew. Chem. Int. Ed.* **64**, e202424098 (2025).
15. Kong, S. et al. Delocalization state-induced selective bond breaking for efficient methanol electrosynthesis from CO_2. *Nat. Catal.* **6**, 6–15 (2023).
16. Liu, Z. et al. Switching CO_2 electroreduction toward ethanol by delocalization state-tuned bond cleavage. *J. Am. Chem. Soc.* **146**, 14260–14266 (2024).
17. He, S. et al. The p-orbital delocalization of main-group metals to boost CO_2 electroreduction. *Angew. Chem. Int. Ed.* **57**, 16114–16119 (2018).
18. Sun, T. et al. Ferromagnetic single-atom spin catalyst for boosting water splitting. *Nat. Nanotechnol.* **18**, 763–771 (2023).
19. Yang, Y. et al. Ligand-tuning copper in coordination polymers for efficient electrochemical C-C coupling. *Nat. Commun.* **15**, 6316 (2024).
20. Lu, T. et al. Local coordination environment-driven structural dynamics of single-atom copper and the CO_2 electroreduction pathway. *J. Am. Chem. Soc.* **147**, 26425–26436 (2025).
21. Lv, X., Liu, Z., Yang, C., Ji, Y. & Zheng, G. Tuning structures and microenvironments of Cu-based catalysts for sustainable CO_2 and CO electroreduction. *Acc. Mater. Res.* **4**, 264–274 (2023).
22. Wang, M. et al. *f-p-d* coupling-induced bonding covalency boosts C–C coupling in electrocatalytic CO_2 reduction over Er–O–Cu sites. *J. Energy Chem.* **108**, 239–245 (2025).
23. Réocreux, R. & Stamatakis, M. One decade of computational studies on single-atom alloys: Is in silico design within reach? *Acc. Chem. Res.* **55**, 87–97 (2022).
24. Greiner, M. T. et al. Free-atom-like d states in single-atom alloy catalysts. *Nat. Chem.* **10**, 1008–1015 (2018).
25. Xu, M. et al. Kinetically matched C-N coupling toward efficient urea electrosynthesis enabled on copper single-atom alloy. *Nat. Commun.* **14**, 6994 (2023).
26. Yang, C.-L. et al. Sulfur-anchoring synthesis of platinum intermetallic nanoparticle catalysts for fuel cells. *Science* **374**, 459–464 (2021).
27. Li, M. et al. Reinforcing Co–O covalency via Ce(4f)–O(2p)–Co(3d) gradient orbital coupling for high-efficiency oxygen evolution. *Adv. Mater.* **35**, 2302462 (2023).
28. Zhu, J. et al. Frustrated Lewis pair mediated f-p-d orbital coupling: Achieving selective seawater oxidation and breaking *OH and *OOH scaling relationship. *Angew. Chem. Int. Ed.* **64**, e202414721 (2025).
29. Zheng, B. et al. Rare-earth doping in nanostructured inorganic materials. *Chem. Rev.* **122**, 5519–5603 (2022).
30. Wang, X. et al. Orbital-level band gap engineering of RuO_2 for enhanced acidic water oxidation. *Nat. Commun.* **16**, 4845 (2025).
31. Franchini, C., Reticcioli, M., Setvin, M. & Diebold, U. Polarons in materials. *Nat. Rev. Mater.* **6**, 560–586 (2021).
32. Zhou, X. et al. Stabilizing Cu^{2+} ions by solid solutions to promote CO_2 electroreduction to methane. *J. Am. Chem. Soc.* **144**, 2079–2084 (2022).
33. Setvin, M. et al. Direct view at excess electrons in TiO_2 rutile and anatase. *Phys. Rev. Lett.* **113**, 086402 (2014).
34. Hao, Y.-N., Chen, T., Zhang, X., Zhou, H. & Ma, Y. Ti-Ti sigma bond at oxygen vacancy inducing the deep defect level in anatase TiO_2 (101) surface. *J. Chem. Phys.* **150**, 224702 (2019).
35. Wang, R. et al. Compressive-strained rutile TiO_2 enables O_2 monohydrogenation for singlet oxygen electrosynthesis. *Nat. Synth.* **4**, 754–764 (2025).
36. Li, R. et al. Strong dipole-promoted N-O bond hydrogenolysis enables ampere-level electrosynthesis of methylamine. *Nat. Chem.* **17**, 1152–1160 (2025).
37. Wu, Q.-J. et al. Atomically precise copper nanoclusters for highly efficient electroreduction of CO_2 towards hydrocarbons via breaking the coordination symmetry of Cu site. *Angew. Chem. Int. Ed.* **62**, e202306822 (2023).
38. Hiramatsu, W. et al. Surface oxygen vacancies on copper-doped titanium dioxide for photocatalytic nitrate-to-ammonia reduction. *J. Am. Chem. Soc.* **147**, 1968–1979 (2025).
39. Kang, S. H. et al. Chemically stable low-dimensional electrides in transition metal-rich monochalcogenides: theoretical and experimental explorations. *J. Am. Chem. Soc.* **144**, 4496–4506 (2022).
40. Li, Y. et al. Recent progress on titanium sesquioxide: Fabrication, properties, and applications. *Adv. Funct. Mater.* **32**, 2203491 (2022).
41. He, Y. et al. In situ fabrication of atomically adjacent dual-vacancy sites for nearly 100% selective CH_4 production. *Proc. Natl. Acad. Sci. USA* **121**, e2322107121 (2024).
42. Wei, Z.-W. et al. Reversed charge transfer and enhanced hydrogen spillover in platinum nanoclusters anchored on titanium oxide with rich oxygen vacancies boost hydrogen evolution reaction. *Angew. Chem. Int. Ed.* **60**, 16622–16627 (2021).
43. Greczynski, G., Haasch, R. T., Hellgren, N., Lewin, E. & Hultman, L. X-ray photoelectron spectroscopy of thin films. *Nat. Rev. Methods Primers.* **3**, 40 (2023).
44. Pauly, N., Tougaard, S. & Yubero, F. LMM Auger primary excitation spectra of copper. *Surf. Sci.* **630**, 294–299 (2014).
45. Wu, T. et al. Identifying the origin of Ti^{3+} activity toward enhanced electrocatalytic N_2 reduction over TiO_2 nanoparticles modulated by mixed-valent copper. *Adv. Mater.* **32**, 2000299 (2020).
46. Shen, Y. et al. Room-temperature photosynthesis of propane from CO_2 with Cu single atoms on vacancy-rich TiO_2. *Nat. Commun.* **14**, 1117 (2023).
47. Zhang, W. et al. Electrolyte design using "Porous Water" for high-purity carbon monoxide electrosynthesis from dilute carbon dioxide. *Angew. Chem. Int. Ed.* **64**, e202424104 (2025).
48. Luc, W. et al. SO_2-induced selectivity change in CO_2 electroreduction. *J. Am. Chem. Soc.* **141**, 9902–9909 (2019).

49. Zhou, B. et al. Electrosynthesis of CO from an electrically pH-shifted DAC post-capture liquid using a catalyst: support amide linkage. *Joule* **9**, 101883 (2025).
50. Li, J. et al. Copper-catalysed electrochemical CO_2 methanation via the alloying of single cobalt atoms. *Angew. Chem. Int. Ed.* **64**, e202417008 (2025).
51. Cai, J. et al. Accurate removal of trace 17β-estradiol and estrogenic activity in blended systems under a photoelectrocatalytic circulating flow. *Environ. Sci. Technol.* **55**, 12585–12595 (2021).
52. Yao, F. et al. Ordered copper triangular atomic sites for industrial-grade electromethanation of CO_2 via self-regulated adsorption of reactants. *Angew. Chem. Int. Ed.* **64**, e202511459 (2025).
53. Zhao, J. et al. Modulation of $*CH_xO$ adsorption to facilitate electrocatalytic reduction of CO_2 to CH_4 over Cu-based catalysts. *J. Am. Chem. Soc.* **145**, 6622–6627 (2023).
54. Ji, Y. et al. Selective CO-to-acetate electroreduction via intermediate adsorption tuning on ordered Cu–Pd sites. *Nat. Catal.* **5**, 251–258 (2022).
55. Malkani, A. S. et al. Understanding the electric and non-electric field components of the cation effect on the electrochemical CO reduction reaction. *Sci. Adv.* **6**, eabd2569 (2020).
56. Green, I. X., Tang, W., Neurock, M. & Yates, J. T. Jr. Spectroscopic observation of dual catalytic sites during oxidation of CO on a Au/TiO_2 catalyst. *Science* **333**, 736–739 (2011).
57. Guan, Y. et al. Exposure of Au atom on Au(111) in metal nanoclusters for pH-universal electrocatalysis. *Angew. Chem. Int. Ed.* **64**, e202508459 (2025).
58. Zhang, L. et al. Oxophilicity-controlled CO_2 electroreduction to C_{2+} alcohols over Lewis acid metal-doped $Cu^{\delta+}$ catalysts. *J. Am. Chem. Soc.* **145**, 21945–21954 (2023).
59. Delmo, E. P. et al. In situ infrared spectroscopic evidence of enhanced electrochemical CO_2 reduction and C-C coupling on oxide-derived copper. *J. Am. Chem. Soc.* **146**, 1935–1945 (2024).
60. Liu, Z. et al. Surface energy tuning on Cu/NC catalysts for CO electroreduction. *ACS Catal.* **12**, 12555–12562 (2022).
61. Gao, J. et al. Solar reduction of carbon dioxide on copper-tin electrocatalysts with energy conversion efficiency near 20%. *Nat. Commun.* **13**, 5898 (2022).
62. Sebastián-Pascual, P. & Escudero-Escribano, M. Surface characterization of copper electrocatalysts by lead underpotential deposition. *J. Electroanal. Chem.* **896**, 115446 (2021).
63. Hao, S. et al. Acid-humidified CO_2 gas input for stable electrochemical CO_2 reduction reaction. *Science* **388**, eadr3834 (2025).
64. Xu, Z. et al. Electroreduction of CO_2 to methane with triazole molecular catalysts. *Nat. Energy* **9**, 1937–1406 (2024).
65. Cai, J., Niu, T., Shi, P. & Zhao, G. Boron-doped diamond for hydroxyl radical and sulfate radical anion electrogeneration, transformation, and voltage-free sustainable oxidation. *Small* **15**, 1970261 (2019).
66. Stoll, S. CW-EPR Spectral Simulations: Solid State. In *Electron Paramagnetic Resonance Investigations of Biological Systems by Using Spin Labels, Spin Probes, and Intrinsic Metal Ions Part A*, 121–142 (Academic Press, 2015).
67. Stoll, S. & Schweiger, A. EasySpin, a comprehensive software package for spectral simulation and analysis in EPR. *J. Magn. Reson.* **178**, 42–55 (2006).
68. Maintz, S., Deringer, V. L., Tchougréeff, A. L. & Dronskowski, R. LOBSTER: a tool to extract chemical bonding from plane-wave based DFT. *J. Comput. Chem.* **37**, 1030–1035 (2016).
69. Nørskov, J. K. et al. Origin of the overpotential for oxygen reduction at a fuel-cell cathode. *J. Phys. Chem. B* **108**, 17886–17892 (2004).

Acknowledgements

We thank the following funding agencies for supporting this work: National Natural Science Foundation of China (No. 22409031, 22306135, 22509185, 22222901, 22175022), Natural Science Foundation of Zhejiang Province (No. LY24B030009, LQN26B030010), the Science and Technology Commission of Shanghai Municipality (No. 23DZ1200800), the National key research and development program of China (No. 2022YFC2904900), the ARC Centre of Excellence for Green Electrochemical Transformation of Carbon Dioxide (CE230100017) funded by the Australian Government, the China Postdoctoral Science Foundation (2025M781024). The XAS research was undertaken on the MEX-1 beamline (23877) at the Australian Synchrotron, part of ANSTO.

Author contributions

X.Lv, F.Huang, and G.Zheng proposed and supervised the project. Z.Liu, J.Cai, and X.Lv designed the experiments. Z.Liu, S.Dong, C.Qin, Z.Lv, J.Wang, and J.Gong performed material synthesis, electrochemical experiments, structural characterizations, and corresponding data processing. X.Lv performed DFT calculations. J.Cai performed the in-situ time-field E-EMR experiments. Y.Yang collected the XAS data, and Z.Liu analyzed the data. G.Zheng, X.Lv, F.Huang, F.Li, and J.Cai acquired funding support for this project. Z.Liu and X.Lv wrote the manuscript; Q.Han participated in the key discussion and revision of the manuscript; Y.Yang, J.Cai, and F.Li contributed to manuscript editing. All the authors discussed the results and provided significant assistance during the manuscript preparation.

Competing interests

The authors declare no competing interests.

Additional information

Supplementary information The online version contains supplementary material available at https://doi.org/10.1038/s41467-026-69260-z.

Correspondence and requests for materials should be addressed to Qing Han, Fuqiang Huang, Ximeng Lv or Guoqu Zheng.

Peer review information *Nature Communications* thanks Shu Ping Lau and the other anonymous reviewer(s) for their contribution to the peer review of this work. A peer review file is available.